Petroleum Science 23 (2026) 7216–7229

Contents lists available at ScienceDirect

Petroleum Science

journal homepage: www.keaipublishing.com/en/journals/petroleum-science

Original Paper

Mechanisms of mobilizing water-sealed residual gas via low-frequency pulsating waves

Jing Liu [a,b,*], Yu-Qian Wang [a,b], Meng-Dong Xing [c], Yi-Qiang Liu [d], Yi-Min Jiang [e], Fei-Peng Wu [a,b]

[a] School of Petroleum Engineering, China University of Petroleum (East China), Qingdao, 266580, Shandong, China
[b] State Key Laboratory of Deep Oil and Gas, China University of Petroleum (East China), Qingdao, 266580, Shandong, China
[c] The Engineering Technology Department of Dagang Oilfield, PetroChina, Tianjin, 300280, China
[d] The Second Oil Production Plant of Dagang Oilfield, PetroChina, Cangzhou, 061103, Hebei, China
[e] Hade Oil and Gas Production Management Area, PetroChina Tarim Oilfield Company, Korla, 841000, Xinjiang, China

ARTICLE INFO

Article history:
Received 20 December 2025
Received in revised form
10 April 2026
Accepted 14 June 2026
Available online 19 June 2026

Edited by Jia-Jia Fei

Keywords:
Low-frequency pulsating wave
Water-sealed residual gas
Disturbance of gas-water interface
Mechanism of action

ABSTRACT

Breaking the gas–water interfacial equilibrium of water-sealed residual gas is critical for improving recovery in water-invaded gas reservoirs. Given the limitations of existing energy-enhancement and displacement technologies, low-frequency pulsating waves can effectively disrupt this mechanical equilibrium through energy superposition and inertial interfacial effects, thus offering an innovative approach for the efficient mobilization of water-sealed residual gas. To elucidate the pore-scale mechanisms by which low-frequency pulsation mobilizes water-sealed residual gas, a customized micro-visualization apparatus was used in combination with pixel-based analysis. This approach enabled high-resolution tracking of the dynamic evolution of the gas–water interface under pulsating conditions, thereby revealing the efficacy and governing mechanisms of pulsation-driven recovery for various residual gas types. Experimental results demonstrate that low-frequency pulsating waves effectively disrupt the gas–water interfacial equilibrium, mobilizing water-sealed residual gas. Under optimal conditions (frequency: 0.1 Hz, amplitude: 12.7 kPa), an overall recovery ratio of 41.98% was achieved, with the recovery ratios for edge band gas and water-blocked gas reaching 69.59% and 35.79%, respectively. Mechanistic analysis indicates that pulsation frequency governs the superposition effect of inertial vibrations at the gas–water interface by modulating the energy supply timing. An optimal frequency range allows subsequent pressure disturbances to intervene prior to the completion of interfacial deformation recovery, inducing net displacement or fragmentation of the isolated gas clusters. Cumulative effects over multiple cycles thereby lead to a marked increase in ultimate recovery. In contrast, pulsation amplitude primarily determines the energy input per cycle, directly controlling the instantaneous degree of interfacial deformation. A higher amplitude is preferable, as it substantially increases deformation within a single cycle, destabilizes the gas–water interface more effectively, and thus elevates the per-cycle recovery efficiency. These findings provide a scientific basis for optimizing process parameters in low-frequency pulsation techniques aimed at enhancing the mobilization of water-sealed residual gas resources.

© 2026 The Authors. Publishing services by Elsevier B.V. on behalf of KeAi Communications Co. Ltd. This is an open access article under the CC BY-NC-ND license (http://creativecommons.org/licenses/by-nc-nd/4.0/).

* Corresponding author.
E-mail address: liujing4522009@163.com (J. Liu).
Peer review under the responsibility of China University of Petroleum (Beijing).

https://doi.org/10.1016/j.petsci.2026.06.023
1995-8226/© 2026 The Authors. Publishing services by Elsevier B.V. on behalf of KeAi Communications Co. Ltd. This is an open access article under the CC BY-NC-ND license (http://creativecommons.org/licenses/by-nc-nd/4.0/).

1. Introduction

Natural gas plays a vital role in the national energy mix, and its efficient exploitation is the key to ensuring stable and growing production of clean energy. Currently, the proven geological reserves of water-drive gas reservoirs in China amount to 5.9×10^{12} m^3. Among these, sandstone gas reservoirs in edge/bottom-water drive systems account for 33.3% of the total, yet their recovery factor is only 16.2%. Such reservoirs therefore represent a primary target for increasing gas reserves and production (He et al., 2023; Hu et al., 2022; Jiang, 2023; Yang et al., 2024). For instance, in the Sebei gas field, continuous gas extraction coupled with strong aquifer influx has led to a sustained decline in reservoir energy and a rapid drop in gas production. Furthermore, long-term water invasion and drainage production measures have led to water-sealed residual gas—primarily in the forms of water-blocked gas, trapped gas, blind-end residual gas, edge water-blocked gas, and edge band gas—reaching a relatively stable gas-water interfacial equilibrium within enriched zones. This stability severely constrains any further enhancement of the recovery factor (Dong et al., 2019; Hu et al., 2014; Liu et al., 2017, Liu et al., 2024; Peng et al., 2021; Tan et al., 2016). Consequently, the key technical challenge in water-invaded zones lies in effectively disrupting this gas–water interfacial equilibrium while replenishing formation energy. Addressing this challenge is imperative to liberate the water-sealed residual gas in fully water-invaded zones of aquifer-driven gas reservoirs and to improve ultimate recovery.

In response to this challenge, research efforts have primarily focused on two approaches: replenishing formation energy and disrupting the gas–water interfacial equilibrium. For replenishing formation energy, various methods have been piloted. For example, in Russia, nitrogen injection has been applied in flooded gas fields such as Medvezhye, utilizing the density difference between nitrogen and methane to create a water barrier and displace residual gas (Adler and Crawford, 1983). In the United States, water injection in the nearly depleted, water-flooded Duck Lake gas reservoir improved the recovery factor by 3.6% (Cason, 1989). In China, water injection tests in the lower aquifer of the Banqiao central condensate gas reservoir yielded certain positive results (Guo et al., 2003). In the study of the Sorrel water-invaded gas field in Tobago, reservoir parameters were determined using the material balance method, and the advantages of water injection versus gas compression were compared (Rambaran et al., 2018). Several scholars have investigated CO_2 injection technology, with the aim of controlling water invasion and enhancing recovery in water-invaded formations (Al-Obaidi et al., 2024; Li et al., 2026; Wei et al., 2025). The successful pilot tests and related studies described above demonstrate that supplementing formation energy can enlarge the macroscopic sweep area and improve gas recovery. However, the established gas–water interfacial equilibrium of water-sealed residual gas cannot be altered, and this type of residual gas cannot be further mobilized. To investigate the gas–water interfacial equilibrium, microfluidic experiments have been widely used to simulate two-phase flow during water invasion. These studies have elucidated the dynamic migration of the interface, the entrapment mechanisms of various water-sealed residual gas types, and factors influencing water invasion. By analyzing pore-scale processes such as spreading, expansion, and coalescence, the key mechanisms leading to interfacial instability have been identified. It is established that the formation of residual gas is governed by the combined effects of hydration forces at the solid–liquid interface, the driving force of invading water, and capillary forces at the gas–water interface. Collectively, this body of work lays the groundwork for disrupting the equilibrium through physicochemical means (Aghaeifar et al., 2019; Huang et al., 2021; Liu et al., 2025; Maaref et al., 2017; Wang et al., 2018; Wang et al., 2021; Wu et al., 2022b; Xu et al., 2021; Yang et al., 2022; Zhang R.H. et al., 2024; Zhang T. et al., 2024). Therefore, exploring a new method that can both supplement formation energy and expand the macroscopic sweep volume, while also disrupting the gas–water interfacial equilibrium to enhance microscopic sweep efficiency, is of great importance for further improving recovery in water-invaded gas reservoirs.

Low-frequency hydraulic pulsation technology converts steady water injection into unsteady injection and establishes an unsteady pressure field within the reservoir, thereby enhancing recovery. In this study, low-frequency hydraulic pulsating waves were investigated with emphasis on the deep superposition effect of pulsation-induced energy and on the progressive inertial deformation and breakthrough of fluid interfaces. This technology is intended to achieve two objectives. On the one hand, formation energy is replenished and macroscopic sweep efficiency is improved. On the other hand, the original mechanical equilibrium of residual gas is disrupted, pore-scale microscopic sweep is enhanced, and the efficient mobilization of water-sealed residual gas is promoted. Owing to these mechanisms, low-frequency pulsating waves have achieved relatively successful field applications in high-water-cut sandstone reservoirs in the Shengli Oilfield (Wu et al., 2022b, 2025). This background leads to a key scientific question: How can such physical waves, under conditions of formation energy replenishment, disrupt the microscopic equilibrium at the gas–water interface and mobilize different types of residual gas. Therefore, based on the mechanism of pulsating water injection, this study investigates the dynamic migration mechanisms that disrupt the gas–water interfacial equilibrium and evaluates the mobilization efficacy for various types of residual gas. To isolate the core microscale physics, experiments were designed by preserving the similarity of key pore-scale forces, such as capillary and interfacial forces, while setting aside complex macroscopic geological structures and high-pressure conditions. A locally heterogeneous glass-etched model was constructed to match the pore-throat characteristics of the target Sebei gas reservoir. Utilizing a micro-visualization setup, we designed and conducted low-frequency pulsation experiments to visualize the mobilization of water-sealed residual gas. The study investigated the migration process under different pulsation parameters, elucidated how these parameters disrupt the gas−water interfacial equilibrium and control its dynamic migration, and deciphered the influence and underlying mechanisms of pulsation frequency and amplitude on the recovery efficiency of various gas types. Furthermore, the recovery ratios of different water-sealed residual gas types under varying pulsation parameters were quantitatively characterized. This work provides key insights and a quantitative basis for assessing the feasibility of this technology and for designing field implementation plans aimed at tapping into water-sealed residual gas resources.

2. Experimental design and methodology

2.1. Experimental apparatus and materials

2.1.1. Experimental device

The microscopic visualization apparatus consisted of four parts: a liquid supply unit, a controllable pulsation generator, a microscopic displacement unit, and an image acquisition unit. The liquid supply unit consisted of adjustable supports and hanging buckets. At the inlet, the pulsation amplitude was adjusted by changing the height of the hanging-bucket support. At the outlet, the pore pressure of the model was controlled in the same manner.

The height control accuracy of the liquid supply unit was 0.1 mm, corresponding to a liquid-column pressure of 9.81 Pa. The controllable pulsation generator consisted of a pulsation switch, a solenoid valve, and hoses. The pulsation frequency was regulated through the solenoid valve, with a control accuracy of 0.001 Hz. The microscopic displacement unit consisted of a glass-etched model and an LED light source. The image acquisition unit consisted of a 928D microscope and an image and data acquisition system. The image acquisition frame rate was 60 fps.

2.1.2. Experimental materials

The exterior size of the microscopic glass etching model used in the experiment was 76 mm × 76 mm (customized in accordance with the pore-throat characteristics of the Sebei gas reservoir), and its effective size was 40 mm × 40 mm. The overall thickness of the model amounted to 5 mm, and its wettability was water-wet (with a wetting angle of 32.5°). The pore diameter range was 10–50 μm. The model exhibited certain local heterogeneity (the pore-throat diameter at the margin of the model was relatively small, ranging from 10 to 30 μm), and the average porosity was 0.3. The experimental water was based on the simulated formation water of the Sebei gas reservoir ($NaHCO_3$ water type, with a salinity of 166658.24 mg·L^{-1}). The gas used in the experiment was methane, and the staining agent used was methyl blue.

2.1.3. Other experimental devices

The experimental setup also included a methane gas cylinder, a vacuum pump, a measuring cylinder, check valves, three-way valves, a pressure gauge, a heating jacket, and a high-temperature and high-pressure clamper.

2.2. Experimental procedures and protocol

2.2.1. Experimental procedure

The experimental process of disturbance by low-frequency pulsating waves: (1) Link up the experimental equipment as shown in Fig. 1 and examine the sealing performance of the experimental device. (2) Use the high-temperature and high-pressure clamper to set the confining pressure at 1 MPa, set the temperature at 50 °C, and adopt the vacuum pump to vacuum and saturate the formation water. (3) Open the methane gas cylinder and inject the gas phase at 0.2 MPa until no more water emerges from the outlet end to create irreducible water saturation. (4) Close the outlet end, and then continue to inject gas into the model. After monitoring that the model pressure stabilizes at 0.2 MPa, stop the gas injection and close the inlet end. (5) Adjust the water-column height at the outlet to 0.1 m, which corresponds to the pore-pressure level of the model. Open the valve switch connecting the outlet end and the check valve until no more gas emerges from the hanging bucket at the outlet end. At this point, the pressure inside the model is the height of the 0.1 m water column +0.1 MPa atmospheric pressure. (6) Open the inlet end of the model connected to the liquid column, turn off the pulsation controller, and conduct stable water flooding at a liquid surface height of 0.7 m (5.9 kPa pressure) until no more gas is discharged from the outlet end to form water-sealed residual gas. Use the image acquisition device to record the static image of the microscopic etched model after water invasion. (7) Turn on the pulsation controller, set the relevant pulsation parameters (adjust the pulsation frequency by regulating the pulsation controller, and set the pulsation amplitude by adjusting the water column height at the pulsation input end), conduct the low-frequency pulsation wave disturbance experiment, and simultaneously use the image acquisition device for real-time video recording until no more gas is discharged from the outlet end. (8) Use the image acquisition device to record the static image at the end of the low-frequency pulsation wave mobilizing the water-sealed residual gas. Process the static images using SAIVER2 and Image-Pro software to obtain the pixels of different types of water-sealed residual gas, and thereby evaluate the effect of the low-frequency pulsation wave mobilizing the water-sealed residual gas. (9) The microscopic glass-etched model was cleaned, and steps (1)–(8) were repeated. At least three experiments were conducted for each parameter condition, and the experimental error was controlled within 5%. The pulsation parameters were then changed, and the experiment was continued.

2.2.2. Experimental protocol

Based on a pulse-wave propagation and attenuation model, the initial pulse amplitude under Sebei reservoir conditions was

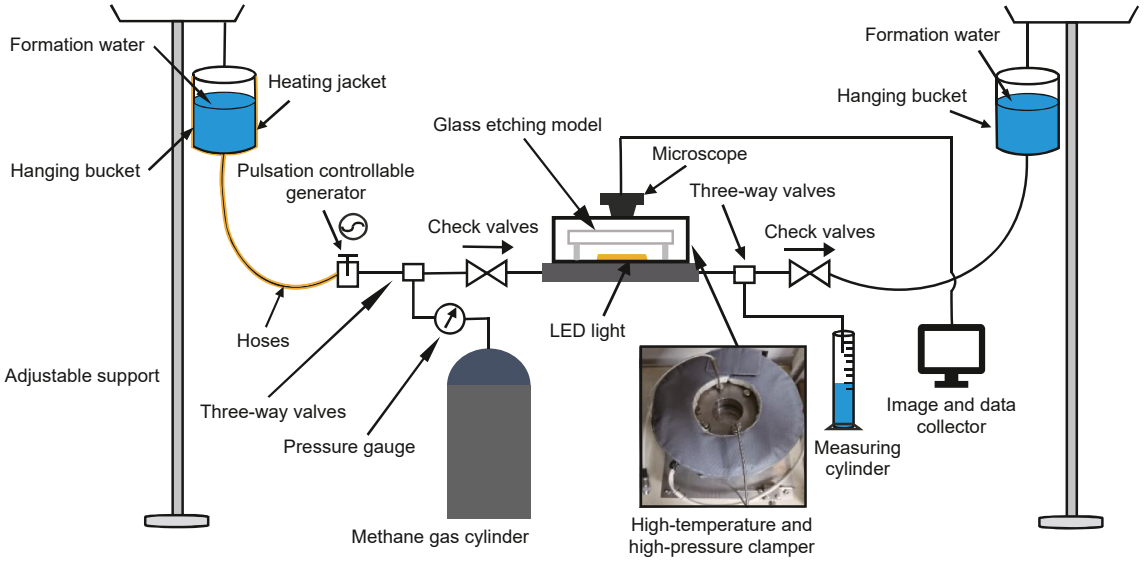


Fig. 1. Flowchart of the low-frequency pulsating wave disturbance experiment.

Table 1
Experimental parameter settings for low-frequency pulsation in mobilizing water-sealed residual gas.

No.	Effect of pulsation frequency				No.	Effect of pulsation amplitude			
	Frequency, Hz	Amplitude, kPa	Inlet height, m	Outlet height, m		Frequency, Hz	Amplitude, kPa	Inlet height, m	Outlet height, m
1	0.01	5.9	0.7	0.1	5	0.1	3.9	0.5	0.1
2	0.05	5.9	0.7	0.1	6	0.1	5.9	0.7	0.1
3	0.1	5.9	0.7	0.1	7	0.1	8.8	1	0.1
4	1	5.9	0.7	0.1	8	0.1	12.7	1.4	0.1

estimated to range from 1 to 5 MPa. At propagation distances of 60–150 m, the pressure amplitude was expected to attenuate to approximately 1–15 kPa (Wu et al., 2022a). Previous evaluations of reservoir tolerance to pulsation further indicated that pressure fluctuations within this range would not damage the reservoir. Therefore, different pulsation frequencies and amplitudes were designed within this range to investigate the effectiveness and mechanisms of low-frequency pulsating waves for the mobilization of water-sealed residual gas. The specific experimental design is detailed in Table 1.

3. Experimental results and discussion

3.1. Occurrence characteristics of water-sealed residual gas after water invasion

In this study, the SAIVER2 software was employed to color-code different types of water-sealed residual gas after water invasion. The pixel counts of each residual gas type before and after pulsation were statistically analyzed using Image-Pro software to characterize their respective proportions. This approach enabled a systematic evaluation of the effectiveness and underlying mechanisms of different low-frequency pulsation parameters on various residual gas types.

Based on the microscopic occurrence states of water-sealed residual gas shown in Fig. 2 and the classification criteria listed in Table 2, water-sealed residual gas can be subdivided into five occurrence types: trapped gas, water-blocked gas, edge water-blocked gas, edge band gas, and blind-end residual gas (Liu et al., 2024). Specifically, trapped gas is mainly located in the throats of strongly swept zones; water-blocked gas resides in the pores of strongly swept zones; edge water-blocked gas occurs within pores of weakly swept zones; edge band gas refers to large clusters of water-sealed residual gas distributed across weakly swept zones; while blind-end residual gas is found in blind-end pores along the model boundaries. The proportions of different water-sealed residual gas types after water invasion are shown in Fig. 3. The results indicate that under the given energy conditions, the dominant forms after complete water invasion are water-blocked gas, edge water-blocked gas, and edge band gas, accounting for 32.33%, 33.51%, and 22.81% respectively. In contrast, trapped gas and blind-end residual gas constitute smaller fractions, at 9.65% and 1.71% respectively.

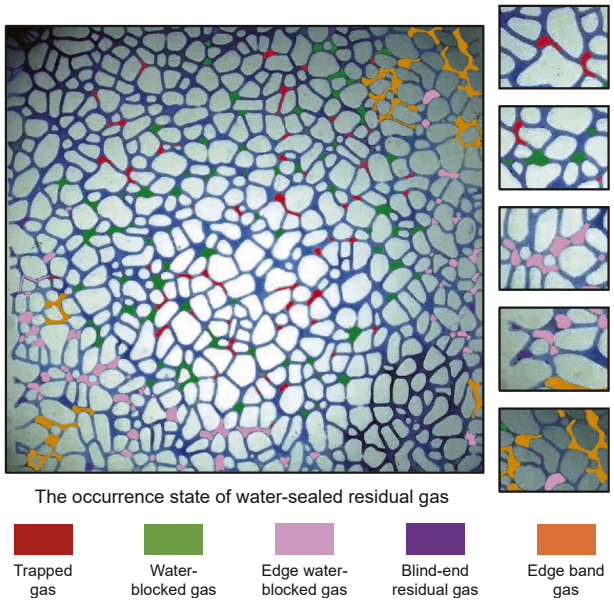


Fig. 2. Microscopic occurrence states and classification of water-sealed residual gas.

3.2. Impact of pulsation frequency on water-sealed residual gas potential tapping

3.2.1. Effect of pulsation frequency on mobilizing water-sealed residual gas

With the pulsation amplitude fixed at 5.9 kPa, a series of micro-visualization experiments were conducted to examine how different frequencies of low-frequency pulsating waves affect the mobilization of water-sealed residual gas. As shown in Fig. 4, the overall recovery ratio initially increases as the pulsation frequency rises from 0.01 to 0.1 Hz, but then gradually declines as the frequency further increases to 1 Hz. Thus, under the given experimental conditions, 0.1 Hz is identified as the optimal frequency, yielding an overall recovery ratio of 18.59%. This analysis suggests that pulsation at 0.1 Hz maximizes the mobilization of water-sealed residual gas, ensuring the most efficient use of the injected energy.

As shown in Fig. 5, both water-blocked gas and edge band gas could be effectively mobilized across the entire tested frequency range (0.01–1 Hz), with their recovery ratios peaking at 0.1 Hz (29.54% and 19.05%, respectively). Trapped gas exhibited only a minor negative recovery (a 2.39% increase in residual saturation) at 0.01 Hz, while it was effectively mobilized within the 0.05–1 Hz range, achieving a recovery ratio of 13.49% at 0.1 Hz. In contrast, blind-end residual gas was mobilized effectively only at 0.1 Hz, with a recovery ratio of 12.66%. At lower frequencies (0.01 and 0.05 Hz), it exhibited substantial negative recovery ratios (−26.83% and −3.44%, respectively). At the higher frequency of 1 Hz, its recovery ratio was merely 0.94%. For edge water-blocked gas, a relatively favorable recovery ratio of 6.51% was obtained at 0.01 Hz, which dropped to 0.51% at 0.1 Hz. Negative recovery occurred at 0.05 and 1 Hz, corresponding to increases in residual saturation of 2.74% and 0.93%, respectively. In summary, a comprehensive analysis of the data indicates that, under the experimental conditions of this study, a frequency of 0.1 Hz enables the efficient mobilization of all types of water-sealed residual gas, thereby maximizing the overall recovery of these trapped resources.

3.2.2. Influence mechanism of pulsation frequency on water-sealed residual gas potential tapping

Pulsation frequency controls the energy-supply timing and thus governs the superposition effect of inertial vibrations at the gas–water interface. As shown in Fig. 5, water-blocked gas and blind-end residual gas exhibit particular sensitivity to pulsation

Table 2
Diagnostic features used to identify five types of water-sealed residual gas.

Type	Geometric location	Dominant trapping mechanism	Diagnostic features
Trapped gas	Narrow throats in strongly swept zones	During water invasion, the continuous gas phase is snapped-off or constricted in narrow throats and becomes isolated there	Mainly occurs in throats; commonly appears as bead-like, elongated, or hammer-shaped gas clusters
Water-blocked gas	Pores in strongly swept zones	Surrounding throats are occupied by the aqueous phase, so the gas is blocked within the pore and cannot be displaced further	Mainly resides inside pores as gas clusters enclosed or surrounded by water
Edge water-blocked gas	Marginal pores in weakly swept zones	Similar to water-blocked gas, but formed in weakly swept marginal regions where water action is weaker and connected throats are fewer and narrower	Mainly distributed in marginal pores; gas clusters have a relatively small contact area with the aqueous phase
Edge band gas	Multiple connected pores and throats along the model edge/weakly swept zones	Due to marginal fine throats, high seepage resistance, and ineffective flow paths, the aqueous phase cannot effectively sweep these regions, leaving connected gas bands behind	Appears as continuous band-like or patchy gas accumulations extending across multiple pores and throats along the model edge
Blind-end residual gas	Blind-end pores near the model boundary	Because of the blind-end geometry and very small local displacement pressure difference, the aqueous phase cannot effectively invade and displace the trapped gas	Located deep in blind-end pores; typically appears as isolated gas trapped in one-end-connected dead-end spaces

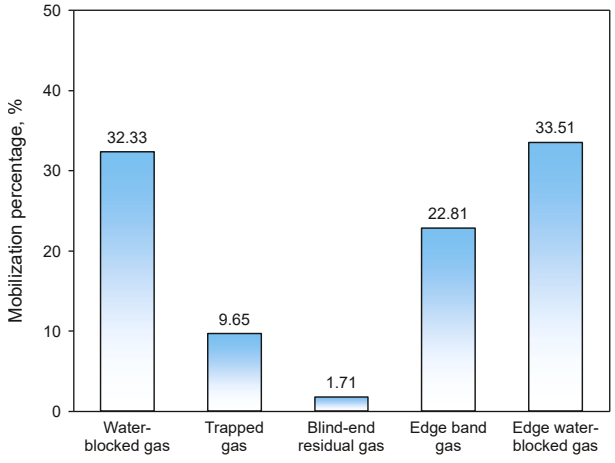


Fig. 3. Proportions of different types of water-sealed residual gas after water invasion.

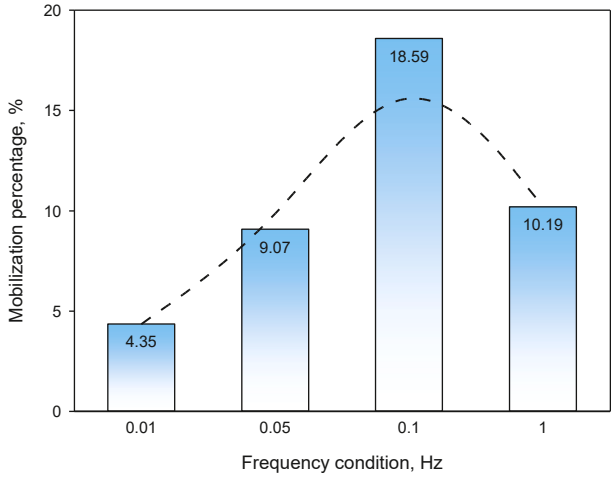


Fig. 4. Effect of frequency on the overall recovery of water-sealed residual gas.

frequency. We therefore analyze the mechanisms through which pulsation frequency mobilizes these two gas types.

(1) Water-blocked gas

The effective mobilization of water-blocked gas requires overcoming the water-blocking effect to enable its entry into the throat. At 0.01 Hz, the gas initially undergoes repeated "deformation–recovery" cycles (Fig. 6(a–c)). The long pulsation period prevents energy superposition, as subsequent pressure disturbances intervene only after complete deformation recovery, thus failing to mobilize the gas efficiently. After approximately 1000 s of pulsation (Fig. 6(d)), prolonged exposure to the unstable pressure field gradually drives the gas into the throat (Fig. 6(e)), but this process is time-consuming and inefficient. At 0.05 Hz (initial state, Fig. 6(f)), after 60 s of pulsation (Fig. 6(g)), the gas overcomes the water-blocking effect and invades the throat during the high-pressure phase, but noticeably retracts in the subsequent low-pressure phase (Fig. 6(h)). With continued pulsation, it gradually advances into the throat (Fig. 6(i) and (j)). At the optimal frequency of 0.1 Hz, the gas effectively accumulates pulsation energy, undergoing repeated expansion and contraction before entering the throat (Fig. 6(k–o)). The required migration time is markedly shorter than at 0.01 and 0.05 Hz. At 1 Hz, rapid pressure alternations disrupt the interfacial force equilibrium, splitting larger bubbles into smaller ones under compression (Fig. 6(p–r)). Some bubbles later coalesce (Fig. 6(s)). However, the high frequency prevents full compression or substantial deformation within a cycle, inhibiting effective energy superposition and resulting in negligible displacement. Larger bubbles become lodged at the throat entrance (Fig. 6(t)), increasing flow resistance. Consequently, water-blocked gas cannot be effectively mobilized at this high frequency.

Force analysis under static equilibrium:

Fig. 7 schematically illustrates the mobilization mechanism of water-blocked gas under pulsating waves. The gas cluster is simplified as a bubble of radius R, surrounded by n throats. Water flows in through some throats and out through others, establishing a static equilibrium (Fig. 7(a)).

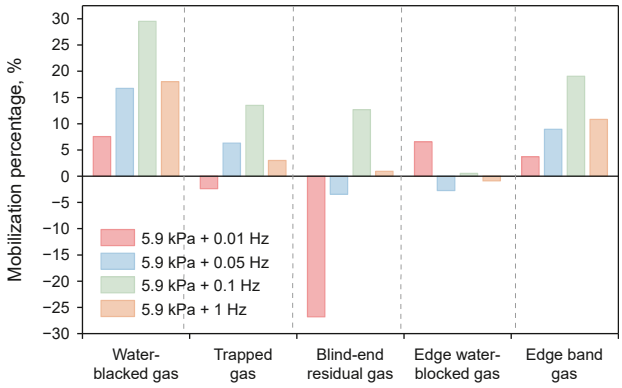


Fig. 5. Effect of frequency on the recovery of different water-sealed residual gas types.

Force analysis of water-blocked gas under static equilibrium:

$$p_g - p_w = p_c \tag{1}$$

where p_g, p_w and p_c represent gas phase pressure, water pressure, and capillary pressure (Pa), respectively.

The capillary pressure is given by:

$$p_c = \frac{2\sigma\cos\theta}{R} \tag{2}$$

where σ is the surface tension (N/m); θ is the contact angle; R is the bubble radius (m).

Dynamic pressure field under pulsation:

The phase difference ϕ caused by wave propagation between two throats separated by distance L is:

$$\phi = \frac{2\pi f L}{v_w} \tag{3}$$

where v_w is the wave propagation velocity in the water phase (m/s).

Under pulsation, the water pressures at throat A and B become time-dependent:

$$\begin{cases} p_{wA}(t) = p_0 + \Delta p\sin(\omega t) \\ p_{wB}(t) = p_0 + \Delta p\sin(\omega t + \phi) \end{cases} \tag{4}$$

where p_0 is the initial pressure (Pa), Δp is the pulsation amplitude (Pa), and $\omega = 2\pi f$ is the angular frequency (rad/s).

As shown in Fig. 7(b), when $\sin(\omega t) = 1$ (high-pressure phase), the phase difference ϕ creates a pressure differential across the

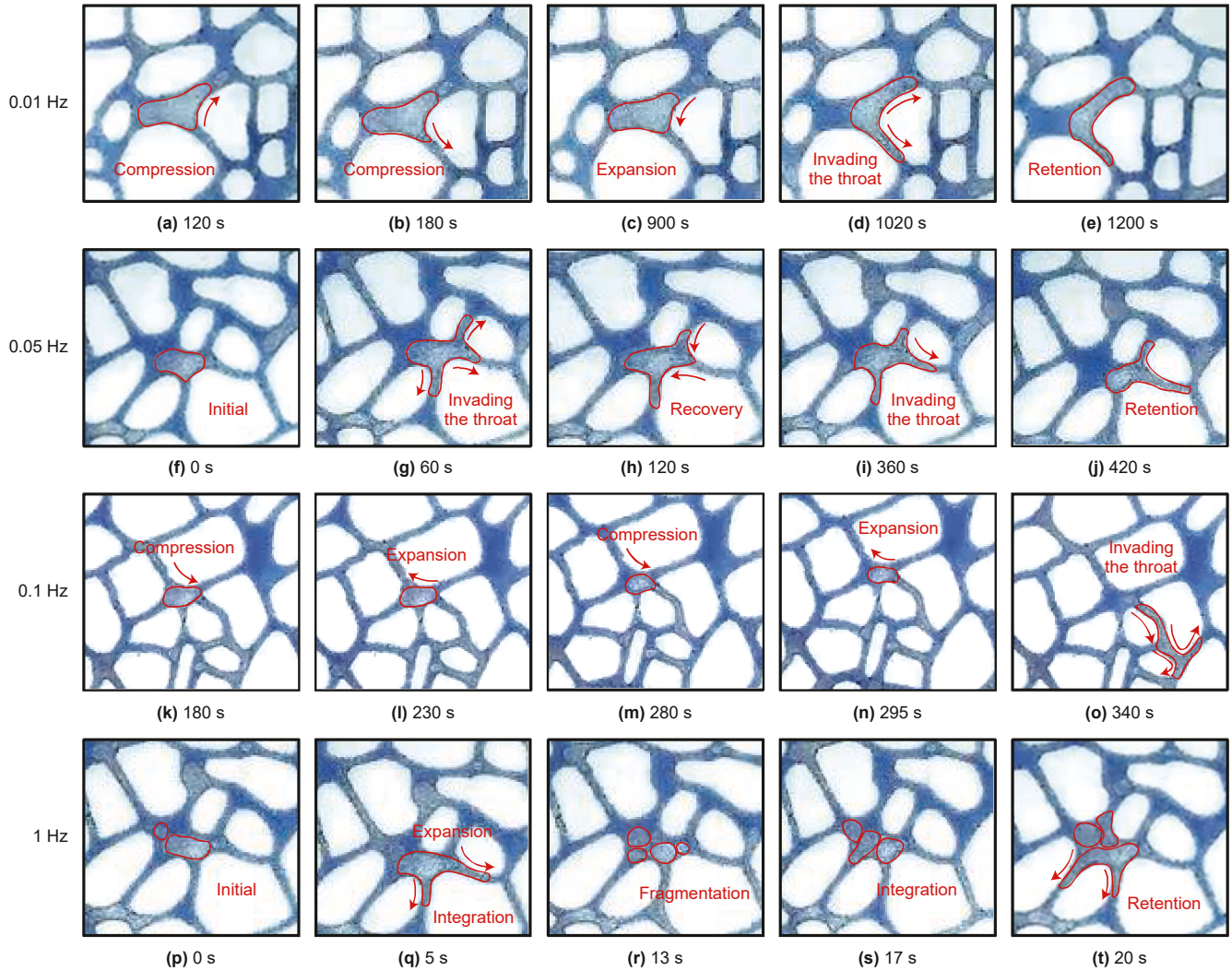


Fig. 6. Mobilization process of water-blocked gas under different pulsation frequencies.

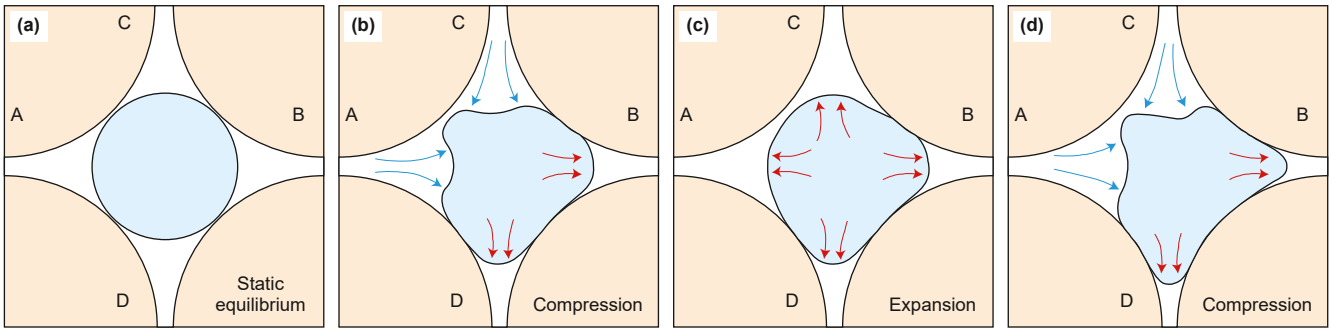


Fig. 7. Mobilization mechanism diagram for water-blocked gas.

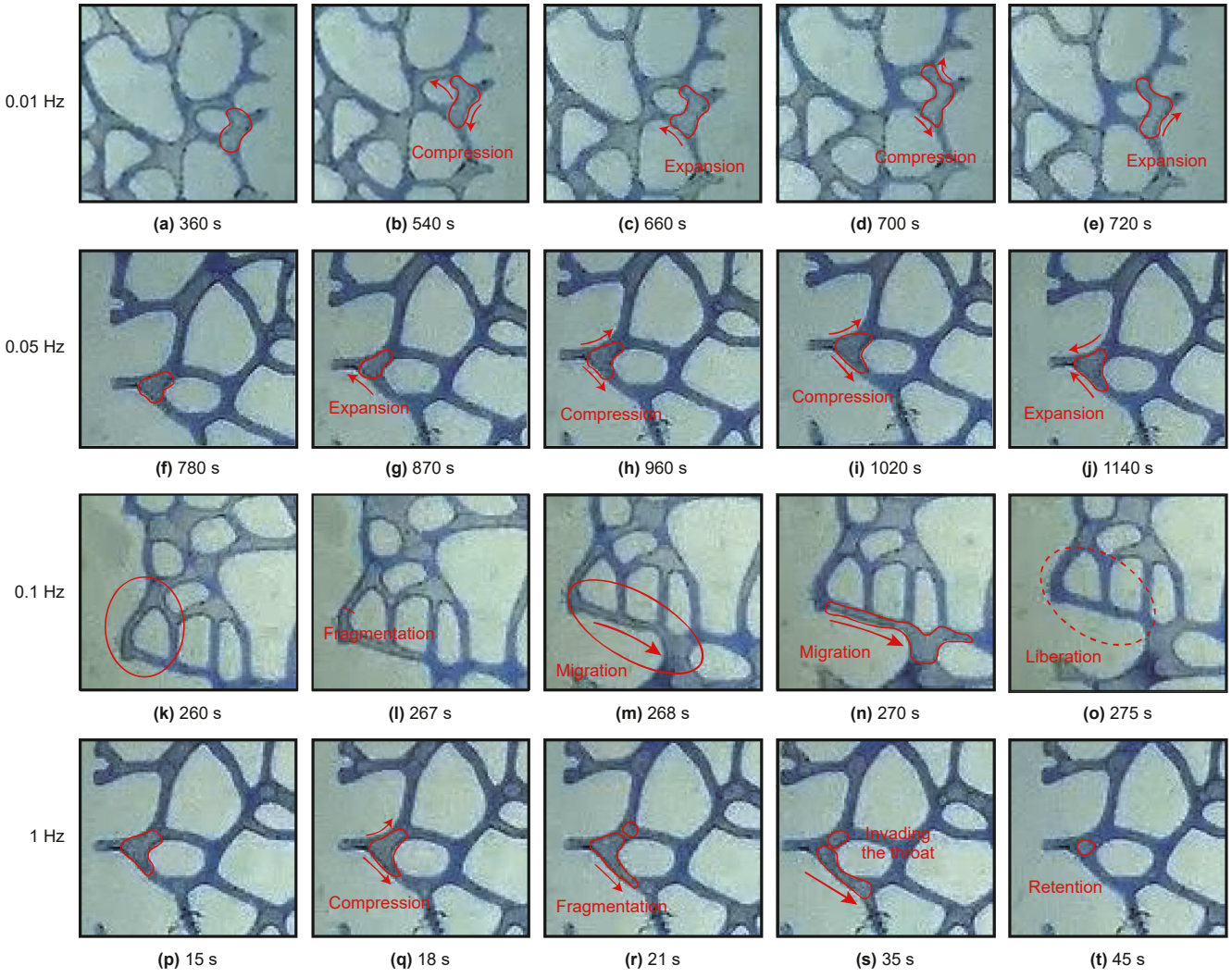


Fig. 8. Mobilization process of blind-end residual gas under different pulsation frequencies.

bubble. This compresses the bubble, causing concave deformation on the high-pressure side and convex deformation on the low-pressure side, initiating throat invasion. When $\sin(\omega t) = -1$ (low-pressure phase, Fig. 7(c)), the bubble expands. At the optimal frequency of 0.1 Hz, the bubble does not fully recover before the next high-pressure phase arrives. This prevents complete retraction and results in a net forward displacement over multiple cycles, enabling the gas to gradually overcome the water-blocking effect and be mobilized.

Meanwhile, taking this water-blocked gas as an example, video recordings obtained at a frequency of 0.1 Hz and an amplitude of 5.9 kPa showed that the contact angle ranged from 158° to 165° after water invasion, whereas under low-frequency pulsation it ranged from 110° to 170°. With an interfacial tension of 55.8 mN/m and a pore-throat diameter range of 10–50 μm for the model, Eq. (2) for capillary force was used for calculation. The capillary resistance after water invasion was calculated to range from 3.79 to 21.56 kPa, whereas under low-frequency pulsation it varied

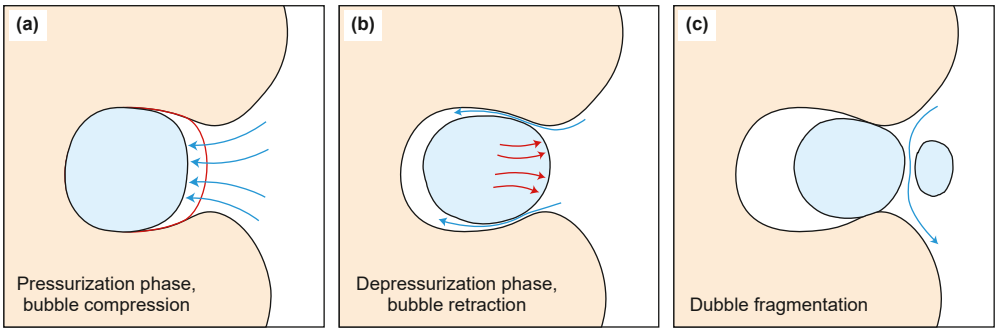


Fig. 9. Mobilization mechanism diagram for blind-end residual gas.

from 1.53 to 21.98 kPa. These results indicate that low-frequency pulsating waves can alter the interfacial configuration of water-sealed residual gas through inertial disturbance and reduce the capillary-resistance threshold required for its breakthrough, thereby promoting the release and migration of water-sealed residual gas.

(2) Blind-end residual gas

The mobilization mechanism of blind-end residual gas relies on the transient accumulation and subsequent release of pulsation energy within large pores. Flow disturbances generated in the main channel create alternating high-pressure and low-pressure zones near blind-end pores. This pressure oscillation drives the aqueous phase from the main channel to gradually invade the blind-end pores, thereby displacing the blind-end residual gas and mobilizing it into the main flow.

At 0.01 and 0.05 Hz, the aqueous phase can displace the blind-end residual gas toward the pore mouth. However, the narrow pore entrance, combined with the delayed replenishment of pulsation energy, causes each subsequent pressure wave to act only after the interfacial deformation from the previous cycle has fully recovered. As a result, the gas remains trapped in a repeated "deformation–recovery" cycle and fails to be mobilized even after prolonged pulsation (Fig. 8(a–e)). Under these low-frequency conditions, blind-end residual gas therefore cannot be effectively mobilized. Moreover, other types of water-sealed residual gas, once disturbed, may migrate into the blind-end pores, thereby increasing the saturation of blind-end residual gas. At the optimal frequency of 0.1 Hz, the gas cluster initially remains stable (Fig. 8(k)). After 267 s of pulsation, it breaks up (Fig. 8(l)) and undergoes cyclic deformation until the aqueous phase invades the blind-end pore and gradually transports the gas toward the outlet. Compared with the lower frequencies, the mobilization efficiency is significantly improved at 0.1 Hz. At 1 Hz, the gas cluster initially present (Fig. 8(p)) breaks up under high-frequency pulsation (Fig. 8(q)). The resulting smaller bubbles can more easily enter the throat and be mobilized (Fig. 8(r)). The remaining larger bubbles are gradually displaced out of the blind-end pore through the "deformation–recovery" cycle, enter the main flow channel, and are subsequently split into multiple smaller bubbles by the aqueous phase (Fig. 8(s) and (t)).

The mobilization mechanism of blind-end residual gas is illustrated in Fig. 9. Under stable waterflooding, the aqueous phase preferentially flows through interconnected pore networks (main flow channels), bypassing blind-end pores. Due to their typical "bottleneck" geometry—narrow entrance and wider interior—a high capillary pressure develops at the throat entrance, inhibiting aqueous phase invasion. Consequently, the gas remains in mechanical equilibrium, as described by Eq. (1), and is effectively trapped within blind-end pores under steady-state conditions.

Under pulsation, the water-phase pressure becomes time-dependent:

$$p_w(t) = p_0 + \Delta p \sin(\omega t) \tag{5}$$

This induces periodic pressure oscillations at the blind-end pore entrance.

The capillary pressure differs during bubble advancement and recession:

$$\begin{cases} p_{c,a} = \dfrac{2\sigma\cos\theta_a}{r_t} \\ p_{c,r} = \dfrac{2\sigma\cos\theta_r}{r_t} \end{cases} \tag{6}$$

where $p_{c,a}$ and $p_{c,r}$ are the advancing and receding capillary pressures (Pa), respectively; θ_a and θ_r are the advancing and receding contact angles; and r_t is the radius of the throat (m).

The critical condition for aqueous-phase invasion into the blind-end pore is:

$$p_w(t) > p_g(t) + p_{c,a} \tag{7}$$

Substituting Eq. (5) yields:

$$p_0 + \Delta p \sin(\omega t) > p_g(t) + p_{c,a} \tag{8}$$

Defining the dimensionless invasion threshold $\eta_1 = [p_{g(t)} + p_{c,a} - p_0]/\Delta p$, Eq. (9) simplifies to:

$$\sin(\omega t) > \eta_1 \tag{9}$$

The time interval satisfying the invasion condition within each cycle is:

$$t \in \left(\frac{\arcsin\eta_1}{2\pi f}, \frac{\pi - \arcsin\eta_1}{2\pi f} \right) \tag{10}$$

The corresponding time proportion is:

$$\beta_1 = \frac{\pi - 2\arcsin\eta_1}{2\pi} \tag{11}$$

Thus, the total time satisfying the invasion condition over n cycles is:

$$t_a = nT\beta_1 = \frac{n}{f}\frac{\pi - 2\arcsin\eta_1}{2\pi} \tag{12}$$

Conversely, the critical condition for bubble migration out of the pore is:

$$p_g(t) > p_w(t) + p_{c,r} \tag{13}$$

Similarly, defining $\eta_1 = [p_{g(t)} - p_{c,a} - p_0]/\Delta p$, the total time satisfying the release condition over n cycles is:

$$t_r = nT\beta_2 = \frac{n}{f}\frac{\pi - 2\arcsin\eta_2}{2\pi} \tag{14}$$

During the pressure-rise phase (Fig. 9(a)), when Eq. (8) is satisfied, the aqueous phase invades the blind-end pore, compressing the gas bubble and raising its pressure. In the subsequent pressure-drop phase (Fig. 9(b)), the water pressure decreases while the gas pressure remains elevated, satisfying Eq. (13) and driving bubble displacement. At the optimal frequency of 0.1 Hz, the bubble curvature can respond promptly to the pressure changes, effectively storing and releasing pulsation energy. Driven by the cyclic pressure differential, the gas undergoes displacement and, after multiple cycles, is mobilized out of the blind-end pore, subsequently split by the aqueous phase, and transported away. Eqs. (12) and (14) show that higher frequencies increase the cumulative time available for displacement, thereby theoretically providing more opportunities for invasion and migration. However, at excessively high frequencies (e.g., 1 Hz), the pressure-change rate becomes too rapid for the gas–water interface to respond fully. This leads to incomplete deformation recovery, bubble rupture, and potential re-trapping at the pore mouth, which ultimately reduces mobilization efficiency.

3.3. Impact of pulsation amplitude on water-sealed residual gas potential tapping

3.3.1. Effect of pulsation amplitude on mobilizing water-sealed residual gas

Microscopic visualization experiments were conducted at a fixed pulsation frequency of 0.1 Hz to investigate the mobilization of water-sealed residual gas by applying low-frequency pulsating waves with varying pressure amplitudes. As shown in Fig. 10, the overall recovery ratio of water-sealed residual gas exhibits a positive correlation with the amplitude. A maximum recovery ratio of 41.98% was achieved at an amplitude of 12.7 kPa, demonstrating that higher amplitude significantly enhances the release of water-sealed residual gas.

As shown in Fig. 11, at a fixed pulsation frequency of 0.1 Hz and an amplitude of 3.9 kPa, all types of water-sealed residual gas were mobilized to varying degrees, except for trapped gas and edge water-blocked gas, which exhibited a negative recovery (i.e., an increase in residual saturation). At higher amplitudes, all gas types were effectively mobilized, with their recovery ratios increasing with amplitude. At the maximum experimental amplitude of 12.7 kPa, the recovery ratios for edge band gas, water-blocked gas, blind-end residual gas, edge water-blocked gas, and trapped gas reached 69.59%, 35.79%, 23.51%, 20.86%, and 20.05%, respectively.

3.3.2. Influence mechanism of pulsation amplitude on water-sealed residual gas potential tapping

Pulsation amplitude primarily controls the degree of deformation at the gas–water interface within a single pulse cycle. Greater deformation more effectively disrupts the interfacial equilibrium. Moreover, a high amplitude generates a strong pressure gradient, which drives the migration of water-sealed residual gas. The impact of amplitude is especially significant for trapped gas and edge band gas (Fig. 11). The mechanism by which amplitude enhances the recovery of these two gas types is analyzed below.

(1) Trapped gas

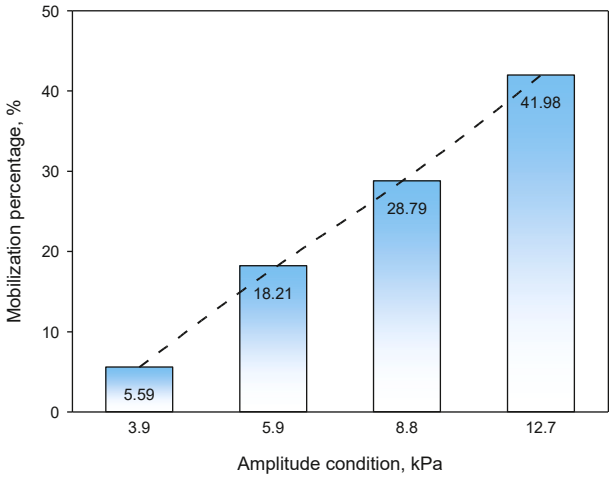


Fig. 10. Effect of amplitude on the overall recovery of water-sealed residual gas.

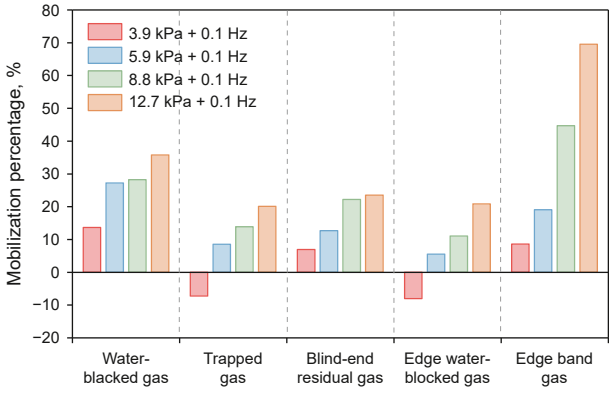


Fig. 11. Effect of amplitude on the recovery of different water-sealed residual gas types.

The mobilization of trapped gas requires overcoming the capillary pressure within pore-throats. At 3.9 kPa, the pulsation energy is markedly insufficient. The gas–water interface experiences only slight disturbance—insufficient to overcome the Jamin effect or to redistribute the pressure field inside and around the bubble. Consequently, the bubble morphology remains largely unchanged (Fig. 12(a–e)). In contrast, other types of water-sealed residual gas undergo limited migration under this weak pulsation; some re-enter throats and become re-trapped, leading to a net increase in trapped gas volume. Therefore, at this amplitude, pulsation has no effective mobilizing effect on trapped gas. At 5.9 kPa, trapped gas exhibits cyclic expansion-compression during pulsation. While bubble geometry gradually couples with the throat boundaries—enabling partial mobilization—the amplitude remains too low to generate sufficient disturbance or local pressure gradient, resulting in low mobilization efficiency (Fig. 12(f–j)). At higher amplitudes of 8.8 and 12.7 kPa, complete mobilization required only 140 and 80 s, respectively. These times are significantly shorter than those at lower amplitudes (>1000 s at 3.9 kPa and 223 s at 5.9 kPa), confirming a positive correlation between displacement efficiency and amplitude. In this high-energy field, bubbles efficiently couple with pulsation energy within few cycles, adapting their shape to the throat curvature. Once the pressure gradient becomes sufficient, the Jamin effect is overcome instantaneously, enabling rapid mobilization from the throat (Fig. 12(k–t)).

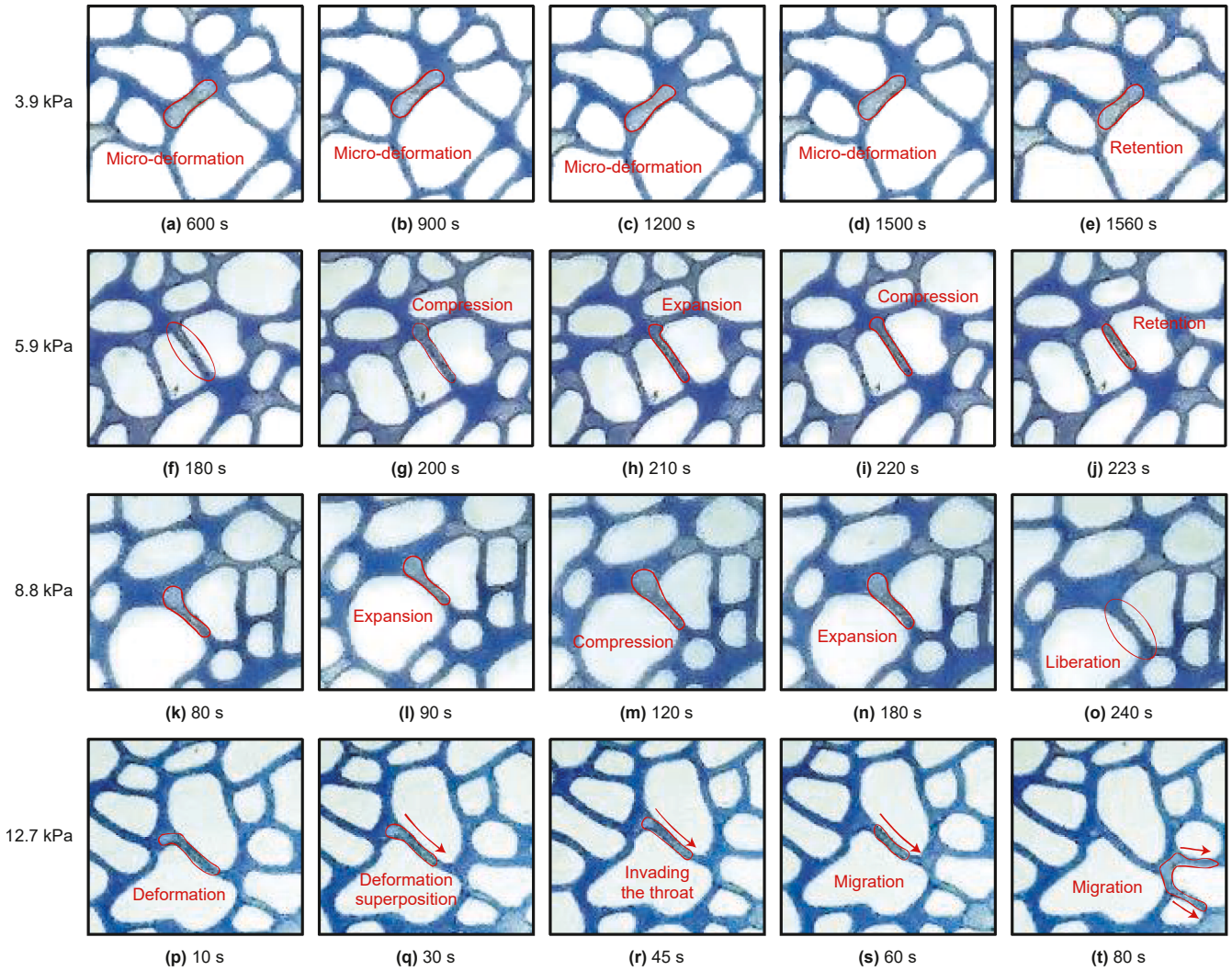


Fig. 12. Mobilization process of trapped gas under different pulsation amplitudes.

In the mobilization mechanism of trapped gas illustrated in Fig. 13, bubble migration is governed by the coupling between periodic pressure fluctuations and contact-angle hysteresis. Specifically, during the pressurization phase, if the local pressure meets Eq. (16), the bubble overcomes capillary resistance and migrates forward; conversely, if the pressure satisfies Eq. (17), the bubble retreats. However, due to contact-angle hysteresis, the difference between the advancing and receding angles introduces asymmetry in bubble migration, which in turn creates a critical pressure window $[p_{c,r} + p_g;\ p_{c,a} + p_g]$. Within this window, the bubble advances during pressurization; during depressurization, the hysteresis effect suppresses its retreat, preventing a return to the initial position and thereby generating net forward displacement. This asymmetric migration behavior accumulates over multiple pulsation cycles, ultimately driving the progressive release of the bubble from the throat and enabling effective mobilization. Further analysis shows that increasing pulsation amplitude enhances the net displacement per cycle, thereby improving mobilization efficiency. Consequently, optimizing pulsation amplitude is a key operational strategy for enhancing trapped-gas recovery.

The forward-migration criterion for water-blocked gas is:

$$p_w > p_{c,a} + p_g \tag{15}$$

The backward-migration criterion for water-blocked gas is:

$$p_w < p_{c,r} + p_g \tag{16}$$

(2) Edge band gas

The poor mobility of edge band gas stems from the widespread micro-throats and inefficient throat networks at the model periphery, which greatly increase water-phase flow resistance and maintain the gas–water system in capillary equilibrium under low-pressure gradients. At a low amplitude of 3.9 kPa, the transient pressure gradient was far below the capillary resistance at the gas–water interface. The interface thus remained in a metastable equilibrium, and the gas morphology showed almost no change (Fig. 14(a) and (b)). With prolonged pulsation, the gas underwent shear-induced destabilization and rupture. However, the low driving-pressure differential remained insufficient to overcome capillary forces. The ruptured bubbles, now with higher curvature, tended to restabilize and remained stranded, preventing effective mobilization (Fig. 14(c–e)). When the amplitude was raised to 5.9 kPa, the local transient pressure gradient first exceeded the

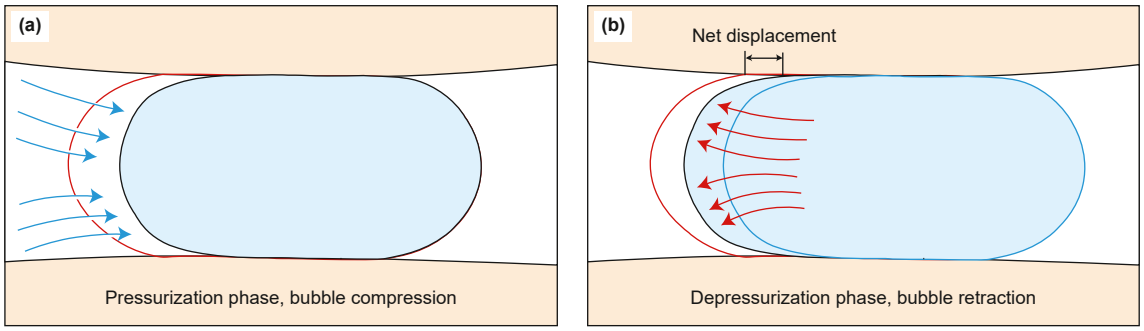


Fig. 13. Mobilization mechanism diagram for trapped gas.

capillary force in one throat, allowing water phase to invade and fragment the gas into multiple bubbles. Bubbles smaller than the throat radius—whose capillary resistance was below a critical threshold—were carried away. The larger bubbles, however, still showed little morphological change under the low-pressure gradient (Fig. 14(f–j)). At 8.8 kPa, the enhanced water-phase pressure differential instantly triggered bubble destabilization, causing rupture within only 5 s. Nevertheless, because the edge band gas is distributed widely across the model periphery, pulsation-wave energy dissipates significantly. The resulting pressure gradient at the edges remained below the displacement threshold, requiring about 1500 s of cumulative pulsation cycles to progressively overcome capillary resistance and produce noticeable macroscopic migration. At the highest amplitude of 12.7 kPa, the pulsation wave instantly breaches the capillary barrier at a throat (Fig. 14(p)). This is accompanied by destabilization and rupture of the gas–water interface (Fig. 14(q)) and water invasion driven by the high displacement pressure differential,

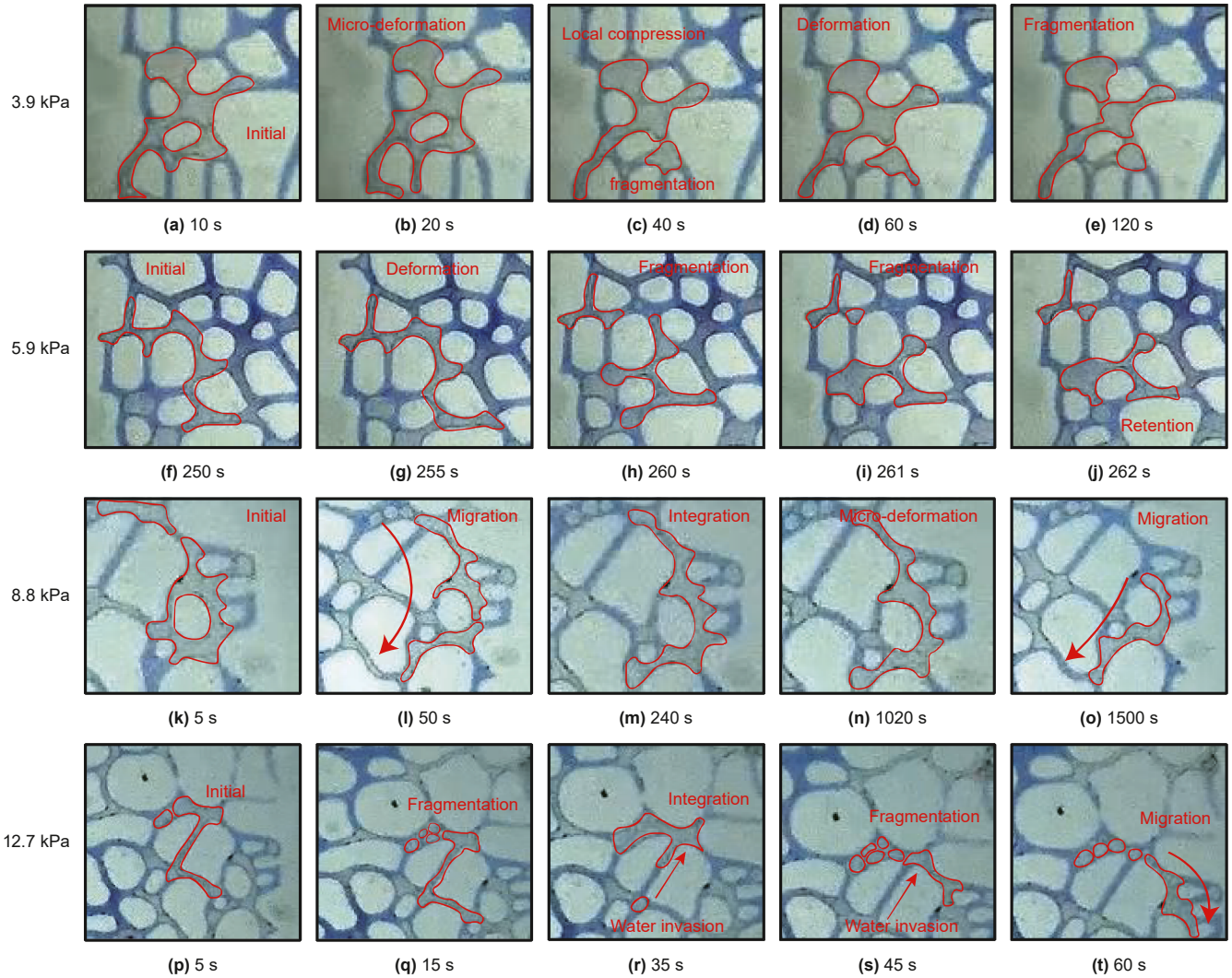


Fig. 14. Mobilization process of edge band gas under different pulsation amplitudes.

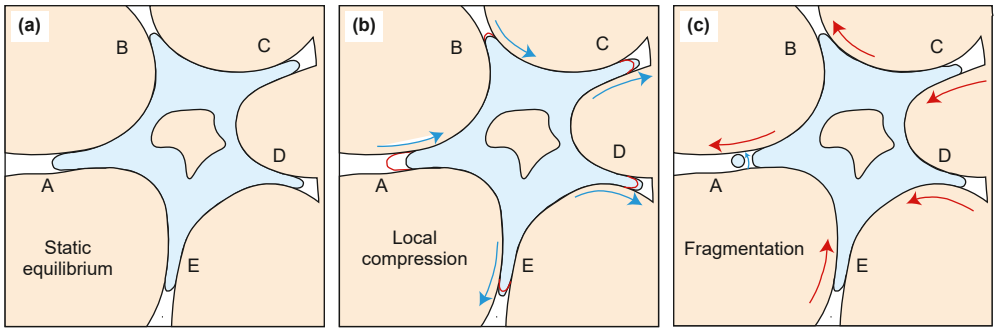


Fig. 15. Mobilization mechanism diagram for edge band gas.

disconnecting the gas phase and ultimately fragmenting the edge band gas into numerous microbubbles (Fig. 14(r) and (s)). Moreover, owing to the elevated pressure gradient, these bubbles exhibit significant displacement within just a few pulsation cycles (Fig. 14(t)).

Under stable waterflooding conditions (Fig. 15(a)), edge band gas—located at the periphery of the model and occupying multiple pore-throats within low-permeability zones—is difficult to be swept. As shown in Fig. 15, edge band gas is trapped by n throats, with the capillary pressure in each throat expressed as:

$$F_{c,i} = p_{c,i} \times A_i = \frac{2\sigma\cos\theta_i}{r_{t,i}} \cdot \pi r_{t,i}^2 = 2\pi\sigma\cos\theta_i r_{t,i} \tag{17}$$

where $F_{c,i}$ is the capillary force (N); A_i is the cross-sectional area (m^2); $r_{t,i}$ is the throat radius (m).

The total capillary resistance is:

$$F_c = \sum_{i=1}^{n} F_{c,i} \tag{18}$$

Under stable flooding, the driving force is lower than F_c, so the gas remains immobilized.

Due to the extensive area occupied by the edge band gas, pulsation-wave propagation requires finite time, leading to a phase lag ϕ_i in water pressure between throats. The time-dependent water pressure at the *i-th* throat is:

$$p_{w,i}(t) = p_0 + \Delta p \sin(\omega t + \phi_i) \tag{19}$$

Under the action of pulsation waves, if a certain throat satisfies the condition $p_{w,i} > p_g + p_{c,i}$, water phase invades, leading to compression of the local gas and a consequent rise in gas pressure. This elevated pressure then drives the adjacent edge band gas, thereby breaking the overall force equilibrium of the edge band gas (Fig. 15(b)). Subsequently, other throats experience rupture due to interfacial instability or water-phase disconnection under continued pulsation. Driven by the pulsation wave, the gas gradually overcomes capillary resistance, detaches from the model periphery, enters the main flow channels, and is thus effectively mobilized (Fig. 15(c)). A higher pulsation amplitude increases the peak water-phase pressure. This higher pressure facilitates meeting the water invasion criterion, induces interfacial instability and rupture, and creates a stronger pressure gradient to drive bubble migration.

3.4. From experiment to field application: conceptual analysis

The foregoing results demonstrate that low-frequency pulsating waves can disrupt the gas–water interfacial equilibrium at the pore-throat scale and effectively mobilize water-sealed residual gas. Under the experimental conditions, the highest recovery of water-sealed residual gas was achieved at an appropriate frequency and a relatively high amplitude. At present, field equipment for hydraulic pulsation tests includes both surface-controlled and downhole-controlled systems. Among them, surface-controlled systems can effectively achieve precise control of both amplitude and frequency. The controllable frequency range is 0.01–35 Hz, and the amplitude range is 0–6 MPa. This technology has already been successfully applied in the Shengli Oilfield for the mobilization of residual oil in high-water-cut waterflooded reservoirs (Wu et al., 2026; Yao et al., 2019). Therefore, for unconsolidated sandstone water-drive gas reservoirs, precise frequency control can already be achieved with current equipment. According to the experimental results, a higher amplitude is generally more favorable. However, in field applications, the amplitude should be determined comprehensively according to the actual operating limits of the equipment, the wellhead pressure tolerance, and the reservoir tolerance. Reservoir tolerance, in particular, is closely related to the long-term effects of pulsating operations on the reservoir skeleton and pore structure, and must be carefully evaluated (Li et al., 2021; Zhang et al., 2026). Therefore, before field application, numerical simulation tools such as ABAQUS should be used to analyze the effects of pulsation parameters on reservoir Young's modulus and Poisson's ratio. These results should then be combined with evaluation indicators such as the degree of sand production and the weakening index of sand production to define the safe ranges of pulsation frequency and amplitude (Liu et al., 2025; Zhai et al., 2023). Based on the above optimization criteria for hydraulic pulsation parameters, a pulsation frequency of 0.1 Hz and an amplitude of 5 MPa are considered suitable for the Sebei gas reservoir.

4. Conclusions

(1) Stable waterflooding at a liquid column height of 0.7 m (5.9 kPa) generated five types of water-sealed residual gas: water-blocked gas (32.33%), trapped gas (9.65%), blind-end residual gas (1.71%), edge water-blocked gas (33.51%), and edge band gas (22.81%). Low-frequency pulsating waves effectively disrupt the gas–water interfacial equilibrium and mobilize these gases. Under optimal conditions (0.1 Hz, 12.7 kPa), the overall recovery ratio reached 41.98%, with individual recoveries of 69.59% (edge band gas), 35.79% (water-blocked gas), 23.51% (blind-end residual gas), 20.86% (edge water-blocked gas), and 20.05% (trapped gas).

(2) Pulsation frequency governs the energy supply timing and thus the superposition effect of inertial vibrations at the

gas–water interface. Water-blocked gas and blind-end residual gas are particularly frequency sensitive. At 0.01 and 0.05 Hz, the long pulsation period prevents energy superposition because subsequent pressure disturbances intervene only after complete interfacial recovery, resulting in limited net displacement and low mobilization efficiency. At 0.1 Hz, pressure disturbances arrive before full recovery, synchronizing and amplifying deformation and displacement to achieve peak energy utilization—an optimal frequency window. At 1 Hz, the disturbance interval (1 s) is shorter than the interface response time. Bubbles experience reverse loading before sufficient deformation, leading to instability or rupture as curvature cannot adjust rapidly. Although some sub throat sized bubbles may be released, most become lodged at throat entrances, hindering further mobilization.

(3) Pulsation amplitude controls the instantaneous degree of interfacial deformation per cycle. Greater deformation more effectively disrupts equilibrium, improving per-cycle efficiency. Trapped gas and edge band gas show strong amplitude sensitivity. At 3.9 and 5.9 kPa, interfacial disturbance is too weak to overcome the Jamin effect. At 8.8 kPa, observable migration begins. At 12.7 kPa, peak water pressure instantly breaches the capillary barrier, destabilizing and fragmenting larger bubbles. Through repeated compression-expansion cycles, bubbles efficiently couple with pulsation energy, adapt their geometry to throat curvature, and are mobilized in a significantly shorter time, substantially enhancing recovery efficiency.

(4) For field implementation of low-frequency pulsating waves to mobilize water-sealed residual gas, both the pore-throat characteristics of the gas reservoir and the occurrence state of water-sealed residual gas should be comprehensively considered, and the pulsation frequency should be determined according to laboratory experimental results. Meanwhile, based on the experimental findings, equipment tolerance, wellhead pressure-bearing capacity, and reservoir protection requirements, the pulsation amplitude should be selected to effectively cover the required pressure window. In this way, the recovery of water-sealed residual gas can be maximized while ensuring economic feasibility, environmental friendliness, and operational safety.

CRediT authorship contribution statement

Jing Liu: Writing – review & editing, Writing – original draft, Methodology, Investigation, Funding acquisition, Formal analysis, Data curation, Conceptualization. **Yu-Qian Wang:** Writing – review & editing, Writing – original draft, Visualization, Methodology, Investigation, Data curation. **Meng-Dong Xing:** Supervision, Investigation, Formal analysis. **Yi-Qiang Liu:** Methodology, Investigation. **Yi-Min Jiang:** Investigation, Data curation. **Fei-Peng Wu:** Validation, Supervision.

Declaration of competing interest

The authors declare that they have no known competing financial interests or personal relationships that could have appeared to influence the work reported in this paper.

Acknowledgments

This work was supported by the National Natural Science Foundation of China, “Investigation into the Mechanism of Enhanced Oil Recovery Using Hydraulic Porosity Dilation Wave in the Late High Water-Cut Stage of Sandstone Reservoir” (No. 52374059), and the China National Petroleum Corporation Science and Technology Special Project, “Research on Enhanced Oil Recovery of Water-Invasion Gas Reservoirs and Development Technology of Low-Abundance Complex Gas Reservoirs” (No. 2021DJ1705).

References

Adler, A.B., Crawford, P.B., 1983. Nitrogen injection into water-driven natural gas or condensate reservoirs increases recovery. In: SPE Annual Technical Conference and Exhibition. SPE-12046-MS. https://doi.org/10.2118/12046-MS.

Aghaeifar, Z., Strand, S., Puntervold, T., 2019. Significance of capillary forces during low-rate waterflooding. Energy Fuels 33 (5), 3989–3997. https://doi.org/10.1021/acs.energyfuels.9b00023.

Al-Obaidi, D.A., Al-Mudhafar, W.J., Hussein, H.H., et al., 2024. Experimental influence assessments of water drive and gas breakthrough through the CO_2-assisted gravity drainage process in reservoirs with strong aquifers. Fuel 370, 131873. https://doi.org/10.1016/j.fuel.2024.131873.

Cason Jr., L.D., 1989. Waterflooding increases gas recovery. J. Petrol. Technol. 41 (10), 1102–1106. https://doi.org/10.2118/12041-PA.

Dong, X.X., Feng, Q.H., Wang, B., et al., 2019. Gas-water percolation law of tight sandstone reservoirs with different pore types in western sulige. Petroleum Geology and Recovery Efficiency 26 (6), 36–45. https://doi.org/10.13673/j.cnki.cn37-1359/te.2019.06.005 (in Chinese).

Guo, P., Li, H.P., Cheng, Y.Z., et al., 2003. Laboratory experiments and field application of water injection for enhanced oil recovery in abandoned condensate gas reservoirs. Nat. Gas. Ind. 23 (5), 76–79+147 (in Chinese).

He, D.B., Jia, A.L., Wei, Y.S., et al., 2023. Theory and technology of balanced development of conventional gas reservoirs. Nat. Gas. Ind. 43 (1), 76–85. https://doi.org/10.3787/j.issn.1000-0976.2023.01.008 (in Chinese).

Hu, Y., Li, X.Z., Jiang, L.J., et al., 2022. Production experiments of multilayer edge-water loose sandstone gas reservoirs in the qaidam Basin. Nat. Gas Geosci. 33 (9), 1499–1508. https://doi.org/10.11764/j.issn.1672-1926.2022.03.009 (in Chinese).

Hu, Y., Li, X.Z., Lu, X.G., et al., 2014. Varying law of water saturation in the depletion-drive development of sandstone gas reservoirs. Petrol. Explor. Dev. 41 (6), 790–793. https://doi.org/10.1016/S1876-3804(14)60094-X.

Huang, X., Zhang, L., Zhang, R., et al., 2021. Numerical simulation of gas-liquid two-phase flow in the micro-fracture networks in fractured reservoirs. J. Nat. Gas Sci. Eng. 94, 104101. https://doi.org/10.1016/j.jngse.2021.104101.

Jiang, S.Y., 2023. Water invasion characteristics and development countermeasures in TY gas field. Master's Thesis, Northeast Petroleum University. https://doi.org/10.26995/d.cnki.gdqsc.2023.000090. (in Chinese).

Li, J., Zhang, X.C., Han, Y.T., et al., 2021. New method to comprehensively predict the sand production risk for unconsolidated sandstone reservoirs and its application. Pet. Geol. Oilfield Dev. Daqing 40 (2), 87–94. https://doi.org/10.19597/j.issn.1000-3754.201912022 (in Chinese).

Li, Z., Hatzignatiou, D.G., Ehlig-Economides, C.A., 2026. Carbon-neutral economic viability of enhanced CO_2 storage and gas recovery in natural gas reservoirs under strong bottom water drive. SPE J. 31 (2), 1305–1320. https://doi.org/10.2118/225593-PA.

Liu, J., Du, J., Ou, B.M., et al., 2024. Occurrence characteristics and formation mechanism of water invaded residual gas in sandstone gas reservoir. Nat. Gas. Ind. 44 (12), 83–93. https://doi.org/10.3787/j.issn.1000-0976.2024.12.008 (in Chinese).

Liu, J., Wang, Y., Dong, X., et al., 2025. Optimal selection of gas-water separation agents and experimental characterization of tapping potential water-sealed gas. ACS Omega 10 (45), 55063–55070. https://doi.org/10.1021/acsomega.5c09711.

Liu, X.J., Xiong, J., Liang, L.X., et al., 2017. Study on the characteristics of pore structure of tight sand based on micro-CT scanning and its influence on fluid flow. Prog. Geophys. 32 (3), 1019–1028. https://doi.org/10.6038/pg20170310 (in Chinese).

Liu, Z., Fan, T., Wang, Z., et al., 2025. A rock brittleness evaluation method in interbedded reservoirs based on statistical damage constitutive. J. Pet. Explor. Prod. Technol. 15 (7), 114. https://doi.org/10.1007/s13202-025-02008-5.

Maaref, S., Rokhforouz, M.R., Ayatollahi, S., 2017. Numerical investigation of two phase flow in micromodel porous media: effects of wettability, heterogeneity, and viscosity. Can. J. Chem. Eng. 95 (6), 1213–1223. https://doi.org/10.1002/cjce.22762.

Peng, X.D., Yang, C.Q., Peng, X., et al., 2021. New understanding about recovery in water drive gas reservoirs: examples from typical ones in western South China Sea. Natural Gas Exploration and Development 44 (2), 36–43 (in Chinese).

Rambaran, K.D., Chin Chee Fat, S.T., Layne, L.E., 2018. Exploiting water injection techniques for increasing gas recovery in conventional gas reservoirs. In: SPE Trinidad and Tobago Section Energy Resources Conference. https://doi.org/10.2118/191206-MS.

Tan, Z.G., Lu, T., Liu, Y.X., et al., 2016. Technical ideas of recovery enhancement in the sulige Gasfield during the 13th Five-Year Plan. Nat. Gas Ind. B 3 (3), 234–244. https://doi.org/10.1016/j.ngib.2016.05.008.

Wang, L., Yang, S.L., Peng, X., et al., 2018. An improved visual investigation on gas-water flow characteristics and trapped gas formation mechanism of fracture-cavity carbonate gas reservoir. J. Nat. Gas Sci. Eng. 49, 213–226. https://doi.org/10.1016/j.jngse.2017.11.010.

Wang, Y.W., Dai, Z.X., Liu, H.Q., 2021. Pore-scale mechanisms and simulations for gas-water two-phase transport processes in natural gas reservoirs. J. Nat. Gas Sci. Eng. 96, 104314. https://doi.org/10.1016/j.jngse.2021.104314.

Wei, J., Zeng, D.Q., Song, Z.J., et al., 2025. Research on CO_2 injection for water control and enhanced nature gas recovery in heterogeneous carbonate reservoirs. Geoenergy Sci. Eng. 244, 213506. https://doi.org/10.1016/j.geoen.2024.213506.

Wu, F.P., Li, N., Sun, D.X., et al., 2022a. Mathematical model of pore pressure transmission law in pulsating water flooding. Journal of China University of Petroleum (Edition of Natural Science) 46 (4), 94–101. https://doi.org/10.3969/j.issn.1673-5005.2022.04.011 (in Chinese).

Wu, F.P., Li, N., Yang, W., et al., 2022b. Experimental characterization and mechanism of hydraulic pulsation waves driving microscopic residual oil. Petrol. Explor. Dev. 49 (6), 1411–1422. https://doi.org/10.1016/S1876-3804(23)60359-3.

Wu, F.P., Song, Y.P., Li, N., et al., 2025. Experimental investigation on enhanced oil recovery by hydraulic pulsating wave driving. Geoenergy Sci. Eng. 244, 213477. https://doi.org/10.1016/j.geoen.2024.213477.

Wu, F.P., Zhang, Y., Jiang, Z.H., et al., 2026. Hydraulic pulsation for enhanced oil recovery in high-water-cut sandstone reservoirs. Phys. Fluids 38, 012118. https://doi.org/10.1063/5.0285411.

Xu, X., Li, X.Z., Hu, Y., et al., 2021. Physical simulation for water invasion and water control optimization in water drive gas reservoirs. Sci. Rep. 11, 6301. https://doi.org/10.1038/s41598-021-85548-0.

Yang, D.S., Xie, K., Yin, Q.G., et al., 2024. Research status and prospect of water intrusion law in edge and bottom water gas reservoirs. Nat. Gas Geosci. 35 (7), 1304–1322. https://doi.org/10.11764/j.issn.1672-1926.2024.01.014 (in Chinese).

Yang, Y.F., Xu, Q.Z., Li, X., et al., 2022. Pore-scale simulation of gas-water two-phase flow in volcanic gas reservoir based on volume of fluid method. J. Nat. Gas Sci. Eng. 106, 104733. https://doi.org/10.1016/j.jngse.2022.104733.

Yao, J.M., Xu, X.M., Liu, Q., 2019. A hydraulic pulse-wave injection-enhancement device. Chinese Patent CN110107258A (in Chinese).

Zhai, M.Y., Li, L.C., Chen, B., et al., 2023. Investigation on the anisotropy of mechanical properties and brittleness characteristics of deep laminated sandstones. Eng. Fract. Mech. 289 (1), 109386. https://doi.org/10.1016/j.engfracmech.2023.109386.

Zhang, R.H., Lu, G., Peng, X., et al., 2024. Study on the mechanism of gas-water two-phase flow in carbonate reservoirs at pore scale. Petroleum 10 (4), 631–645. https://doi.org/10.1016/j.petlm.2023.09.008.

Zhang, T., Zhou, H.J., Zhang, L.H., et al., 2024. Pore-scale investigation of bottom water invasion dynamics in carbonate gas reservoirs with different interlayer distributions. Nat. Gas Ind. B 11 (2), 140–153. https://doi.org/10.1016/j.ngib.2024.04.001.

Zhang, W.H., Tian, S.C., Xia, Y., et al., 2026. Experimental study on sand production characteristics of gas storage under cyclic loading. Petroleum Drilling Techniques 54 (2), 1–10. https://doi.org/10.11911/syztjs.2025136 (in Chinese).